A sensitivity study based on 2D synthetic data from the Gullfaks Field, using PP and PS time-lapse stacks for fluid-pressure discrimination

2006 J. Geophys. Eng. 3 314

(http://iopscience.iop.org/1742-2140/3/4/003)

INSTITUTE OF PHYSICS PUBLISHING JOURNAL OF GEOPHYSICS AND ENGINEERING
J. Geophys. Eng. **3** (2006) 314–328 doi:10.1088/1742-2132/3/4/003

A sensitivity study based on 2D synthetic data from the Gullfaks Field, using PP and PS time-lapse stacks for fluid-pressure discrimination

A Stovas[1], **M Landrø**[1] **and B Arntsen**[2]

[1] Department of Petroleum Engineering and Applied Geophysics, NTNU, 7491 Trondheim, Norway
[2] Statoil Research Centre, Trondheim, Norway

Received 2 June 2006
Accepted for publication 30 August 2006
Published 29 September 2006
Online at stacks.iop.org/JGE/3/314

Abstract
We investigate how combined use of time-lapse PP and PS seismic stacks can be utilized for discrimination between pressure and saturation changes. The theory is based on a combination of the well-known Gassmann and Hertz–Mindlin models. To simulate the amplitudes on PP and PS sections we compute the stacked reflection coefficients within a given angular span. Cross-plotting the PP and PS amplitude changes against the pressure and saturation changes, enables simultaneous estimation of pressure and saturation changes. The method is tested on a realistic 2D finite-difference time-lapse seismic dataset from the Gullfaks Field. The uncertainties in the estimated saturation and pressure changes are expressed by the uncertainties in PP and PS stack amplitudes. We find that this method is strongly dependent on the *in situ* stress conditions, and especially that low values for the initial effective pressure mean low discrimination sensitivity.

Keywords: 4D, PP and PS stacks, fluid-pressure discrimination

Introduction

During the last 5 years several methods for fluid-pressure discrimination from time-lapse seismic data have been suggested. Lumley and Tura (1999) proposed an inversion method for discrimination between pressure and saturation changes based on time-lapse AVO data. The first step is to invert for relative changes in P- and S-wave impedances from the relative changes in the time-lapse AVO data. A second optional step is to use log data to obtain absolute P- and S-wave impedances from the relative changes. Finally, time-lapse changes in impedances are related to time-lapse changes in reservoir properties using impedance cross-plotting. Landrø (1999, 2001) derived explicit equations relating pressure and saturation changes directly to time-lapse amplitude changes in near and far offset stacked data. The necessary inputs to the method are empirical rock physics equations relating

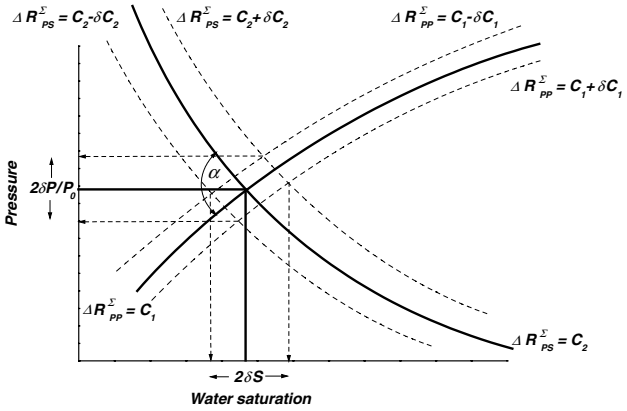

Figure 1. Discrimination between the pressure and saturation changes from the changes in PP and PS amplitudes with definition of angle α and uncertainties in water saturation and pressure.

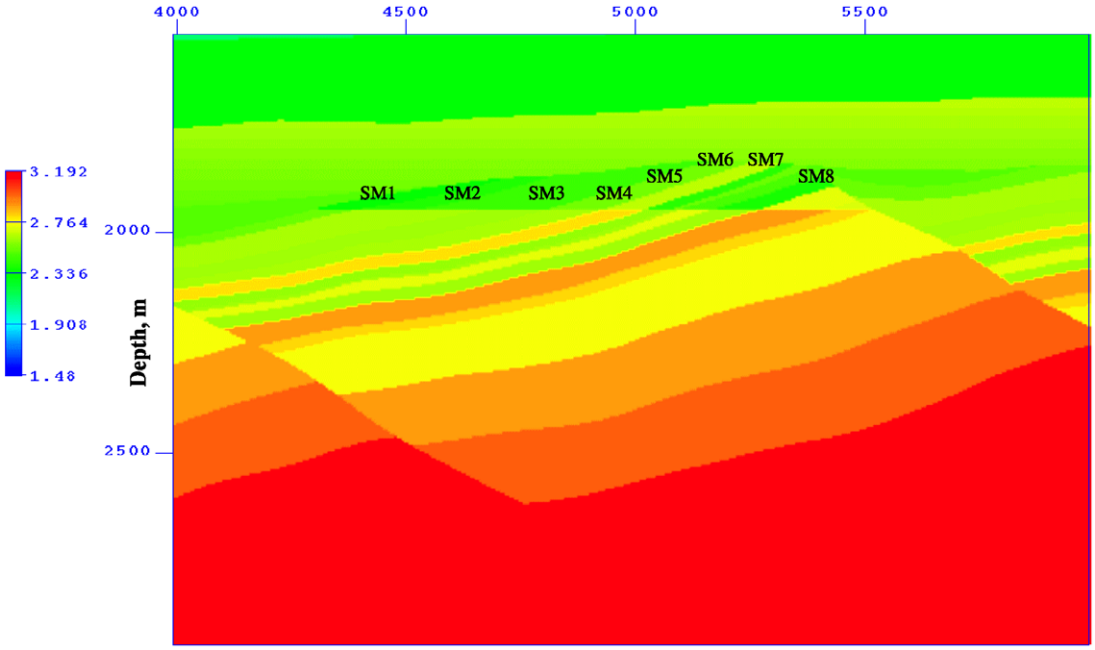

Figure 2. P-wave velocity reservoir model. The reservoir units are indicated as SM1–SM8.

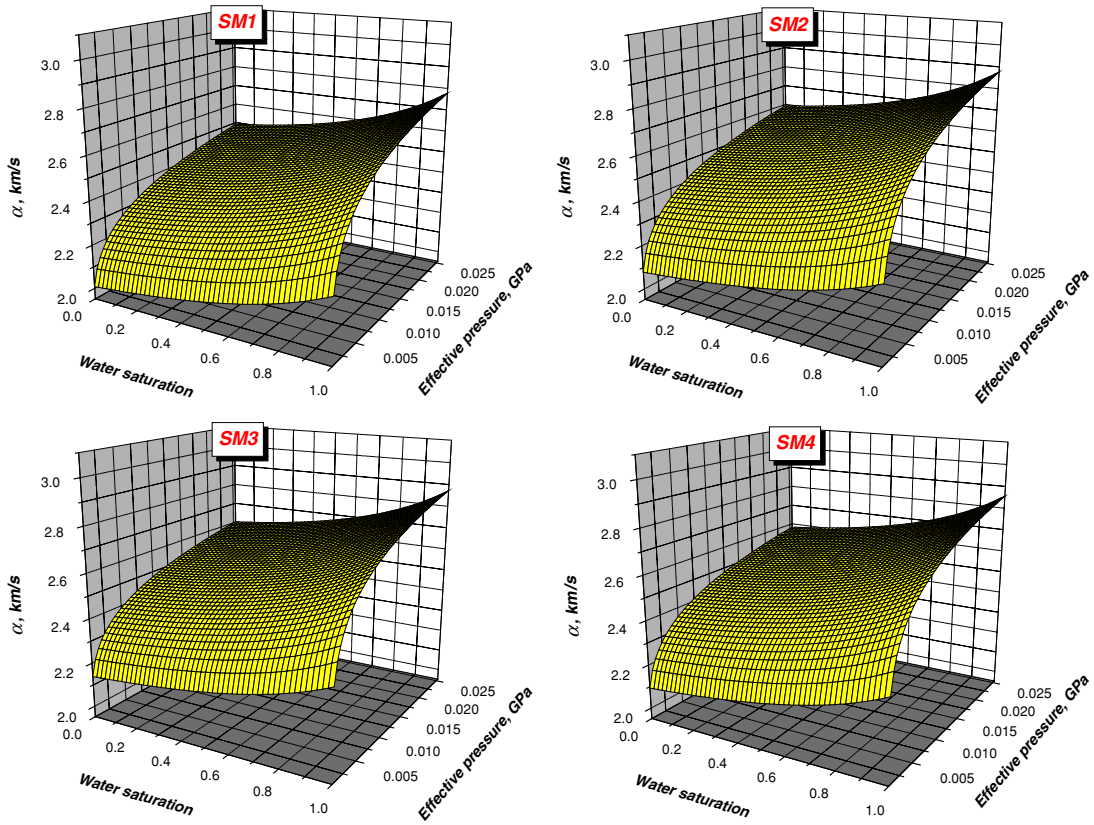

Figure 3. P-wave velocities versus water saturation and effective pressure (Tarbert formation).

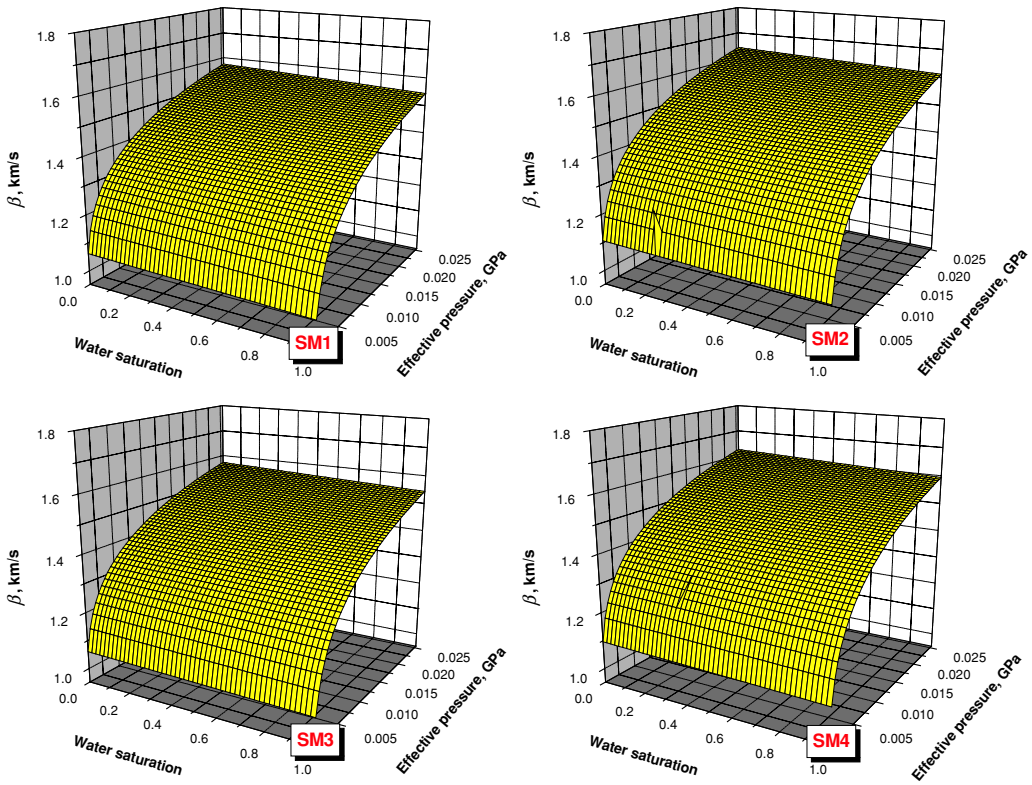

Figure 4. S-wave velocities versus water saturation and effective pressure (Tarbert formation).

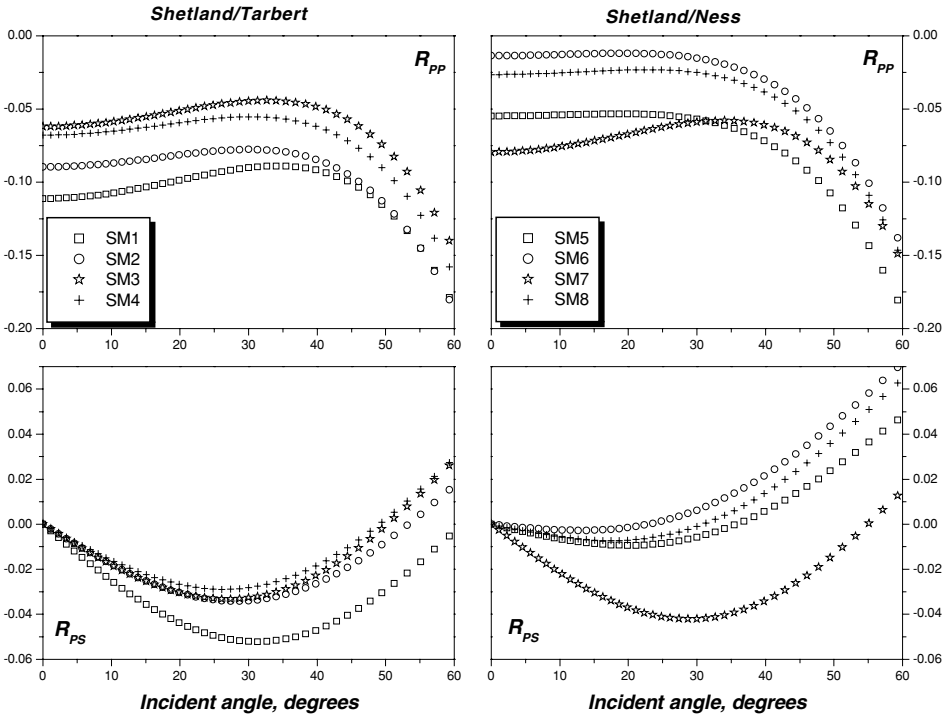

Figure 5. PP and PS reflection coefficients versus P-wave incident angle from interfaces between the Shetland formation and reservoir rocks (Tarbert and Ness formations, model I).

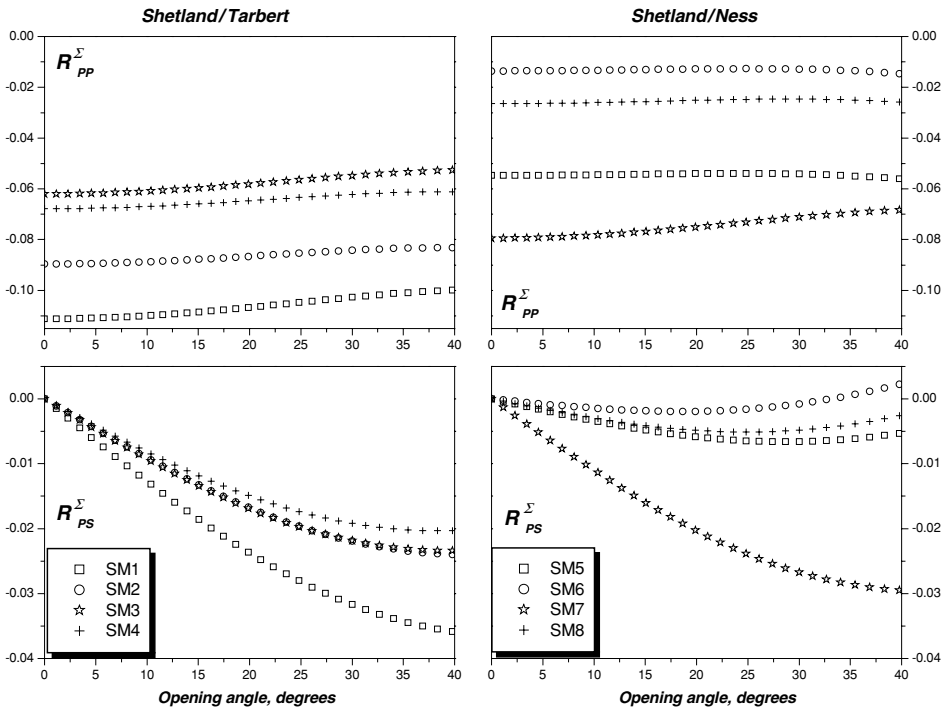

Figure 6. PP and PS stacked reflection coefficients versus P-wave angular span from interfaces between the Shetland formation and reservoir rocks (Tarbert and Ness formations, model I). Note that the PS stacked reflection coefficient is much more sensitive to angular span than the PP stacked reflection coefficient.

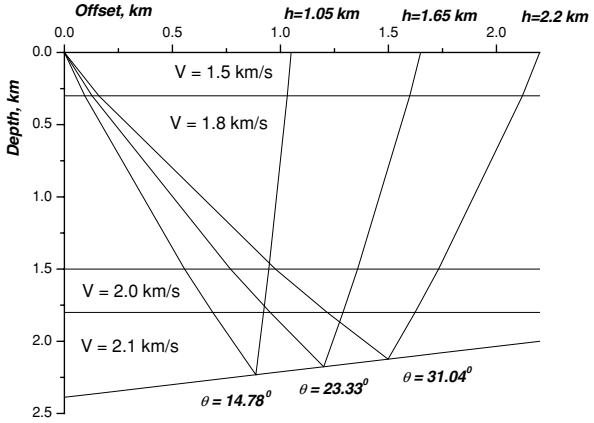

Figure 7. PP ray tracing to estimate the maximum incident angle at the top reservoir.

changes in P-wave, S-wave velocities and densities to changes in pore pressure and saturation. For saturation changes, the commonly used equations are the Gassmann equations. For pressure changes, ultrasonic core measurements or models such as for instance the Hertz–Mindlin model (Mindlin 1949) are used to get this information. In this paper we use 'effective pressure' notation which is defined as the difference between vertical confining stress and pore pressure.

The Gullfaks time-lapse study (Landrø *et al* 1999) and the Draugen time-lapse study (Koster *et al* 2000) show that this qualitative technique has given very useful results for improved reservoir management. Another case study in which pressure effects dominated is the Magnus time-lapse study (see Watts *et al* (1996) and Ritchie *et al* (2002)).

A complementary method to achieve quantitative information about reservoir property changes during production is to measure the shift in the seismic two-way traveltime within a given reservoir section. A practical example of how this method can be used to give additional information about pressure and saturation changes in reservoir segment is given in Landrø *et al* (2001). The repeatability issue is discussed in Landrø (1999), Andorsen and Landrø (2000) and Meunier *et al* (2001). An alternative empirical approach to pressure–saturation inversion is suggested by MacBeth *et al* (2006) and Floricich *et al* (2005).

Measurements of traveltime shifts can be used to estimate the change in, for instance, pay thickness, or amount of pore pressure changes. Combined with estimated time-lapse amplitude changes, the additional traveltime information can be used to constrain and increase the accuracy when estimating various production-related effects simultaneously. Another way of exploiting traveltime shifts is proposed by Guilbot and Smith (2002), where time shifts are used to estimate the degree of compaction in a highly porous chalk field.

In this paper we use the method described in Stovas and Landrø (2004) on a synthetic time-lapse seismic dataset from the Gullfaks Field. To date, there are very few repeated multicomponent seismic surveys, and therefore the most practical way to test our proposed method is to use synthetic data based on the input from a producing field. A similar approach was used in Brevik (1999) and for anisotropic reservoir rocks in Stovas and Landrø (2005).

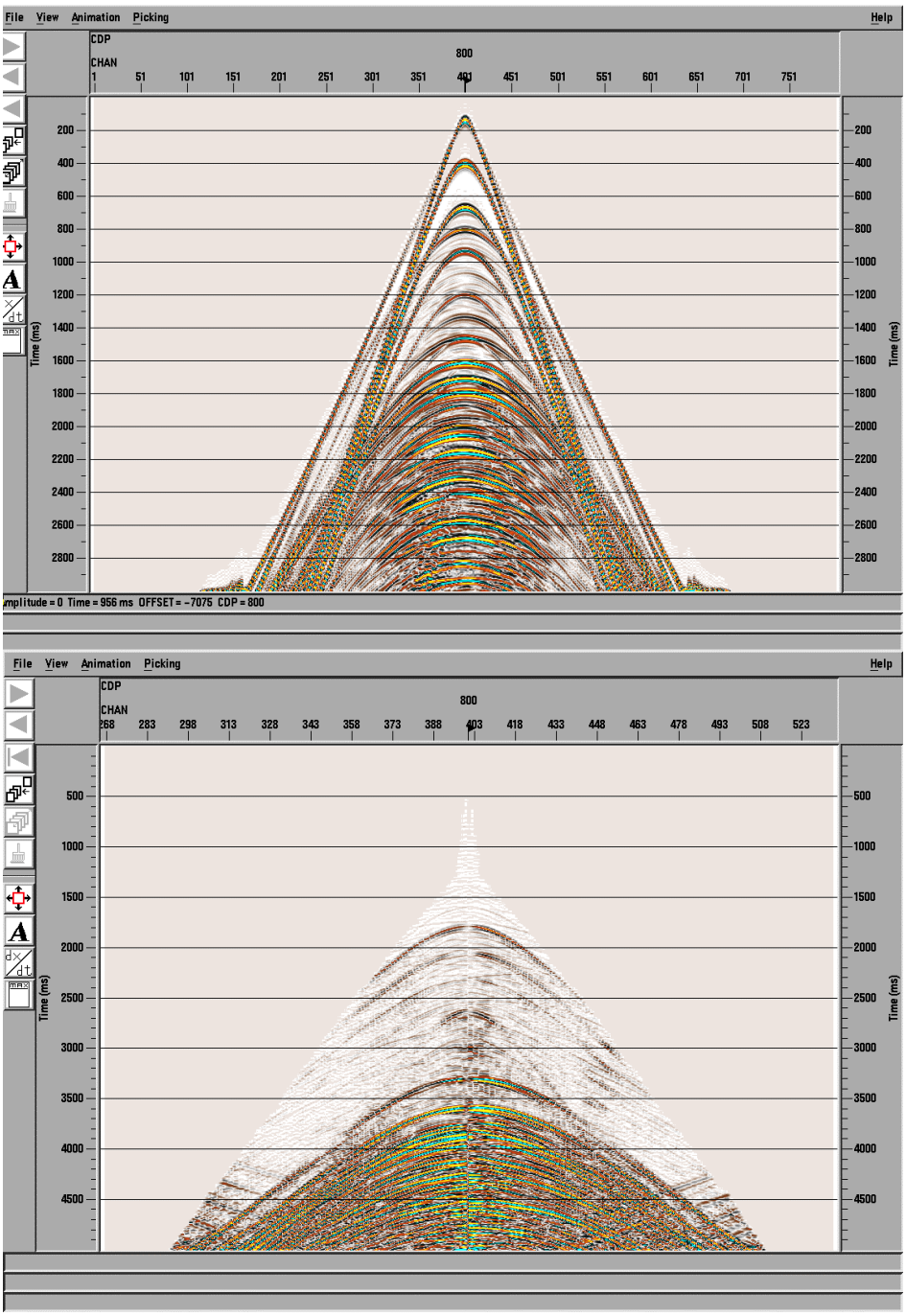

Figure 8. PP (to the top) and PS (to the bottom) CMP gathers from the seismic line.

Here we combine time-lapse PP and PS stacks for optimal discrimination between pressure and saturation effects. We will use the Gassmann model (Gassmann 1951) to describe fluid saturation changes and the Hertz–Mindlin model (Mindlin 1949) to describe pore pressure changes. The procedure to combine these models and their validity are discussed, for example, in Stovas and Landrø (2004). We assume that the models are sufficiently correct to be used for our purpose: to study the applicability of the proposed method with respect to robust (although the synthetic dataset contains the 'the processing noise' only) estimation of pressure and saturation changes.

The stacked reflection coefficients

To simulate the PP and PS amplitudes on seismic stacks we use the stacked reflection coefficients. To compute them we integrate the reflection over the given angle span. For that

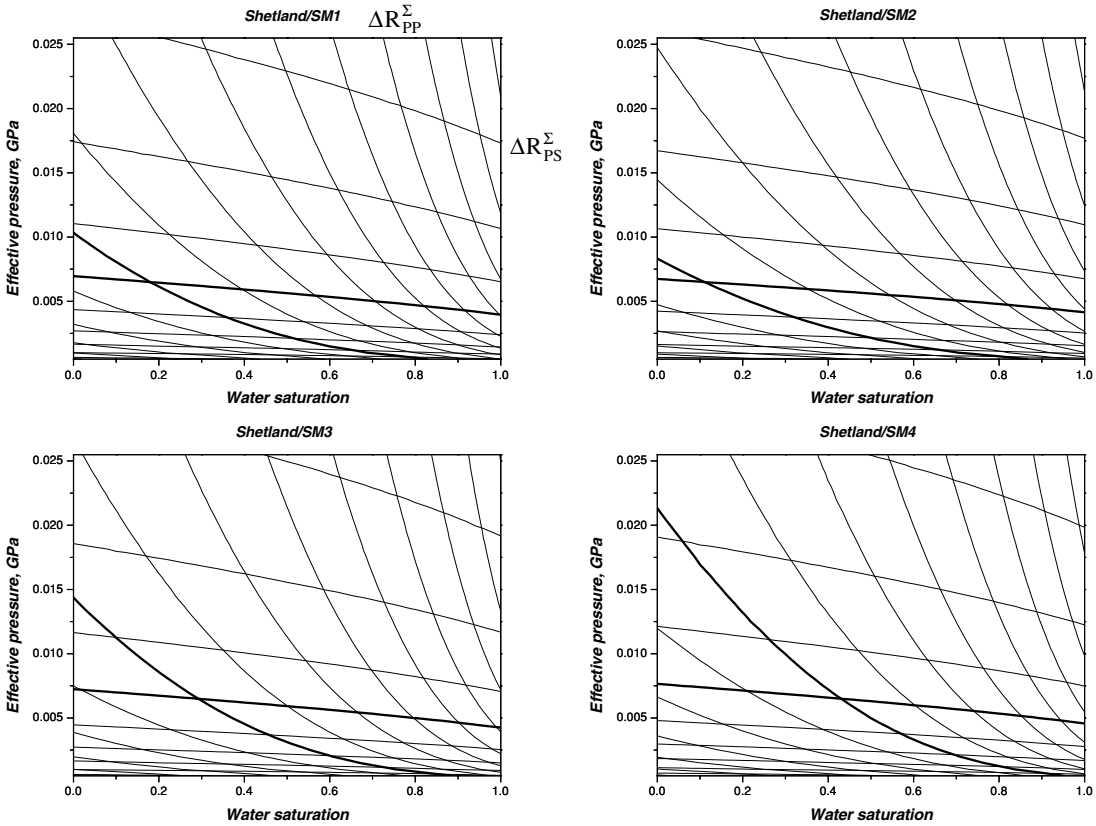

Figure 9. $\Delta R^{\Sigma}_{PP} - \Delta R^{\Sigma}_{PS}$ reflection patterns for the top reservoir. Zero changes in PP and PS amplitudes shown by bold lines. The contour intervals are 0.001 and 0.0002 for PP and PS stacked reflection coefficient, respectively. Positive changes are to the top right from zero change.

purpose we use the angular span between the maximum and minimum incidence angles. We believe that this is the best way to analyse the amplitudes on the stack, not to use the zero-offset reflection coefficient (which, for example, for the PS case is zero). It would be more precise to compute the reflection coefficients for a given set of offsets, but here we would prefer for a sensitivity study to use a more robust approach due to the higher signal-to-noise ratio on the stacked seismic section. Another reason is that the stacked reflection coefficient is less sensitive to uncertainty in elastic parameters. One more assumption of this approach is that the NMO is applied correctly regardless of the non-hyperbolicity of the traveltime curve. In practice it is never possible and, therefore, results in the processing noise in the stacked data.

Weak-contrast reflection coefficients (Ursin and Stovas 2002) will be used in the sensitivity analysis, while exact reflection coefficients from Zoeppritz equations will be used for the saturation–pressure discrimination.

Discrimination between water saturation and pressure changes from PP and PS stacks

In this section we will follow the results from Stovas and Landrø (2004).

First we establish the relationship between the changes in saturation–pressure and the changes in the PP–PS reflection coefficients:

$$\begin{pmatrix} \Delta R^{\Sigma}_{PP} \\ \Delta R^{\Sigma}_{PS} \end{pmatrix} = \begin{pmatrix} b_{11} & b_{12} \\ b_{21} & b_{22} \end{pmatrix} \begin{pmatrix} \Delta S \\ \Delta P/P_0 \end{pmatrix}, \tag{1}$$

where the changes in the normalized stacked reflection coefficients are assumed to be the result of changes in saturation (ΔS) and pressure (ΔP):

$$\Delta R^{\Sigma}_{PP(PS)} = R^{\Sigma}_{PP(PS)}(S + \Delta S, P + \Delta P) - R^{\Sigma}_{PP(PS)}(S, P), \tag{2}$$

and the transformation matrix $\mathbf{B}_{\Sigma} = \begin{pmatrix} b_{11} & b_{21} \\ b_{12} & b_{22} \end{pmatrix} = \mathbf{B}_{\Sigma}(S, P)$. This transformation matrix represents the linear operator, which maps the input vector of the change in saturation and pressure into the output vector of the change in PP and PS seismic amplitudes. The expressions for the elements b_{ij} are given in Stovas and Landrø (2004). Σ means that the reflectivity has been summed over a given offset (or angle) integral. This means that we assume that ΔR^{Σ}_{PP} and ΔR^{Σ}_{PS} represent changes in the corresponding stacked reflection strengths.

The reliability of discrimination between water saturation and pressure changes depends on the angle α between isolines

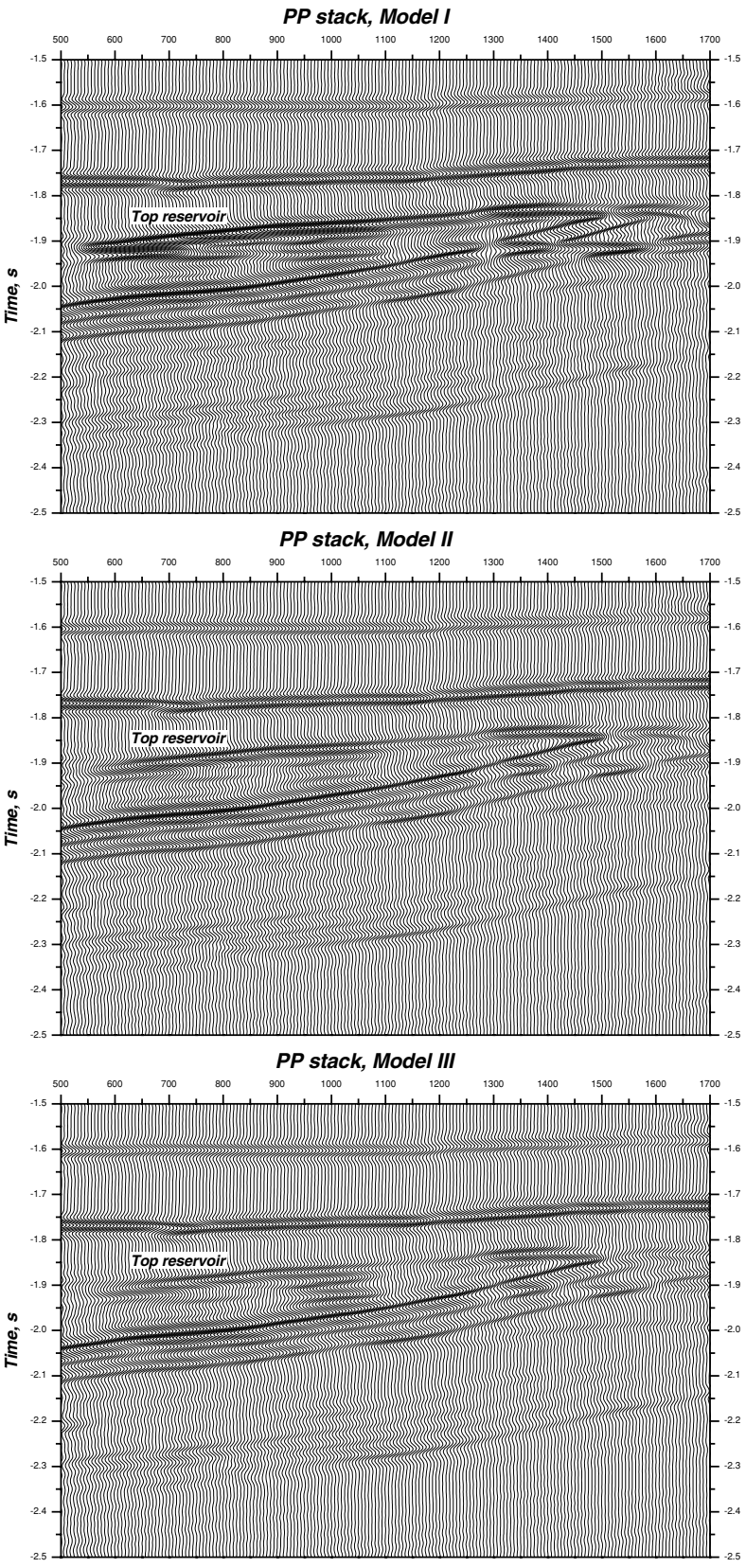

Figure 10. PP stacks computed for models I, II and III.

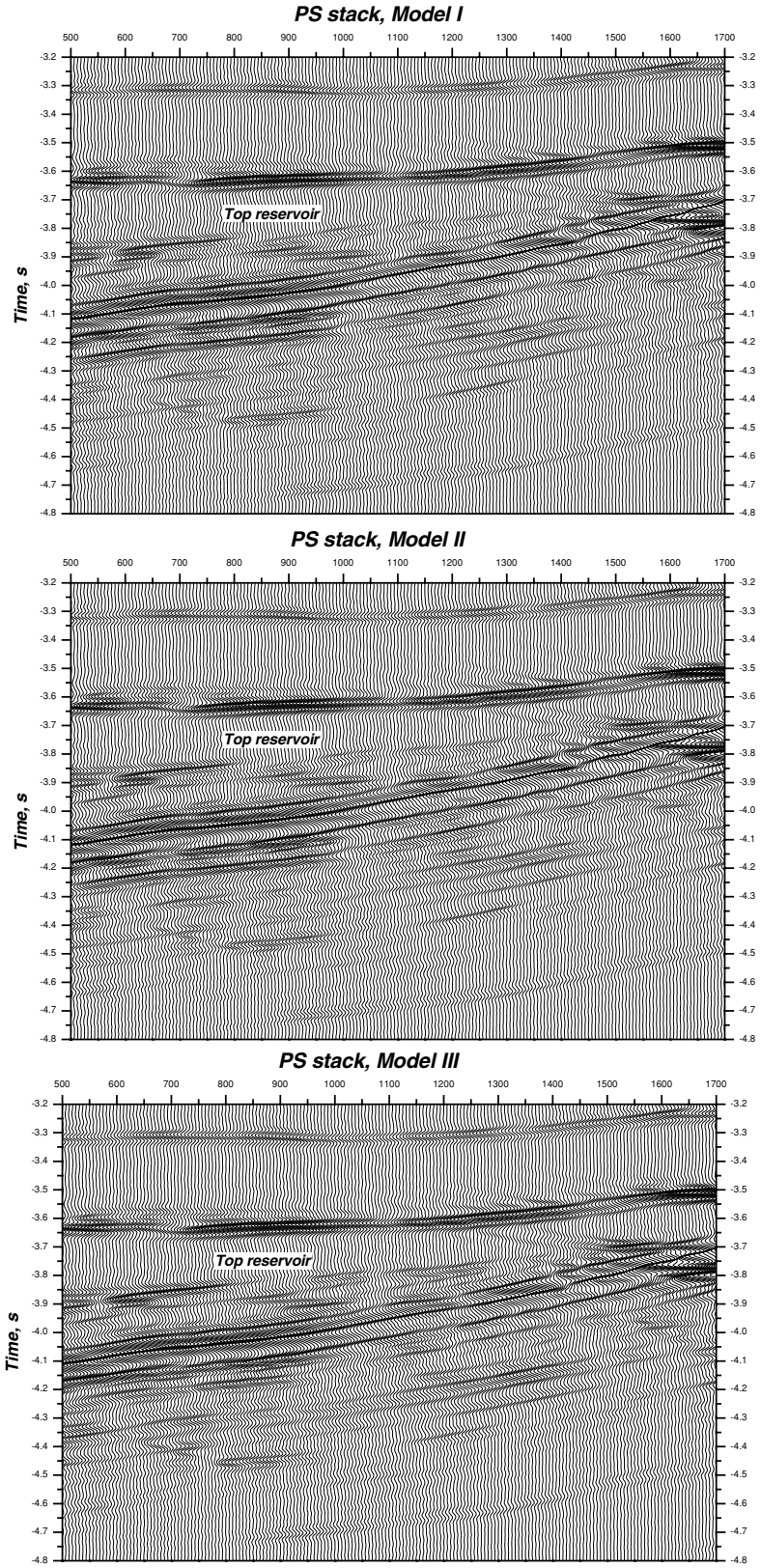

Figure 11. PS stacks computed for models I, II and III.

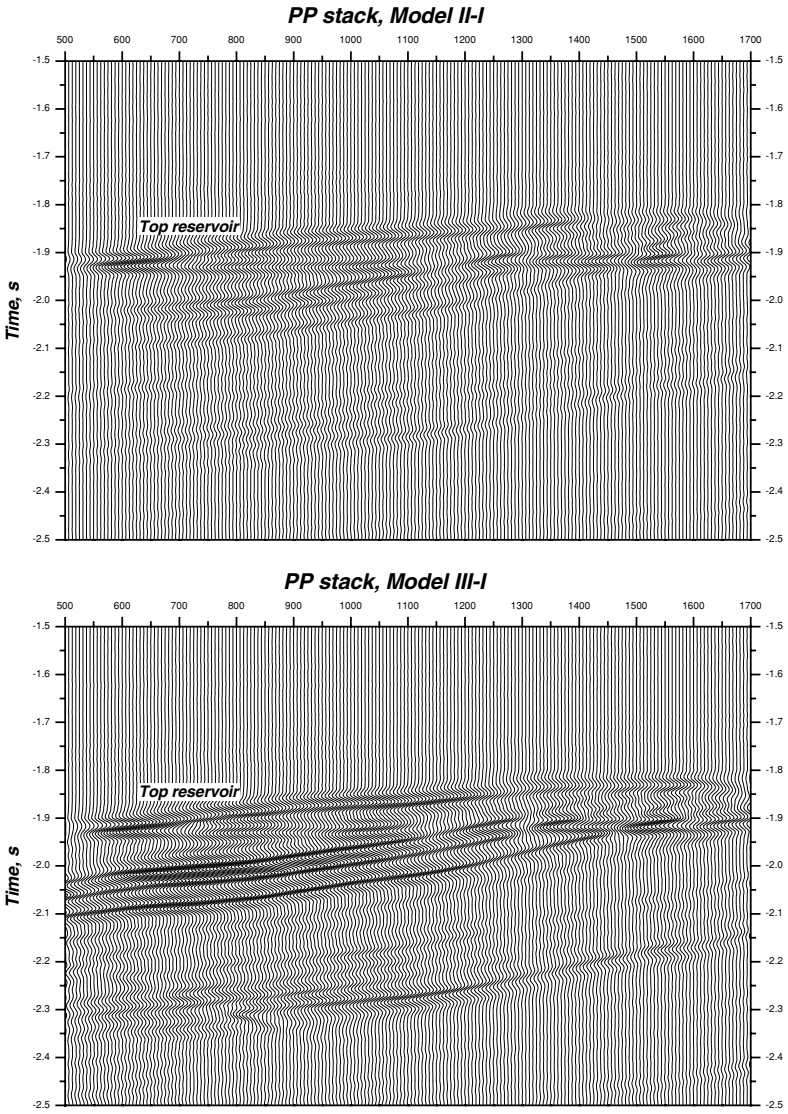

Figure 12. Difference plot for PP stacks from models II and I (to the top) and models III and I (to the bottom).

$\Delta R^{\Sigma}_{\mathrm{PP}} = C_1$ and $\Delta R^{\Sigma}_{\mathrm{PS}} = C_2$ (see figure 1), where C_1 and C_2 are given constants (Stovas and Landrø 2004). The uncertainties in the changes in the PP and PS stacks are related to the uncertainties in fluid saturation and pressure changes.

Inverting equation (8) results in

$$\begin{pmatrix} \Delta S \\ \Delta P/P_0 \end{pmatrix} = \mathbf{B}^{-1}_{\Sigma} \begin{pmatrix} \Delta R^{\Sigma}_{\mathrm{PP}} \\ \Delta R^{\Sigma}_{\mathrm{PS}} \end{pmatrix}, \tag{3}$$

where

$$\mathbf{B}^{-1}_{\Sigma} = \frac{1}{\det \mathbf{B}_{\Sigma}} \begin{pmatrix} b_{22} & -b_{12} \\ -b_{21} & b_{11} \end{pmatrix}. \tag{4}$$

This means that the weighting factors between PP and PS stacks are directly given by the inverse matrix defined in equation (4). Therefore, the uncertainties in fluid saturation and pressure changes ($\delta(\Delta S)$ and $\delta(\Delta P)/P_0$, respectively) can be expressed from uncertainties in PP and PS stack amplitudes ($\delta R^{\Sigma}_{\mathrm{PP}}$ and $\delta R^{\Sigma}_{\mathrm{PS}}$, respectively), with the assumption that if all uncertainties are small, we get

$$\delta(\Delta S) = \frac{1}{\det \mathbf{B}_{\Sigma}} \left(b_{22}\delta\left(\Delta R^{\Sigma}_{\mathrm{PP}}\right) - b_{12}\delta\left(\Delta R^{\Sigma}_{\mathrm{PS}}\right)\right) \tag{5}$$

$$\frac{\delta(\Delta P)}{P_0} = \frac{1}{\det \mathbf{B}_{\Sigma}} \left(-b_{21}\delta\left(\Delta R^{\Sigma}_{\mathrm{PP}}\right) + b_{11}\delta\left(\Delta R^{\Sigma}_{\mathrm{PS}}\right)\right). \tag{6}$$

Uncertainties coupled to the Gassmann and Hertz–Mindlin models are neglected in this study. A more detailed discussion of this issue can be found in Landrø *et al* (2002).

In figure 1 we show how the uncertainties in the PP and PS stack amplitudes relate to the uncertainties in the estimated fluid saturation and pressure changes. Note that the discrimination criteria defined by the discrimination angle α and the relation between the uncertainties in amplitudes and fluid-pressure conditions depend on the values for fluid saturation and pressure.

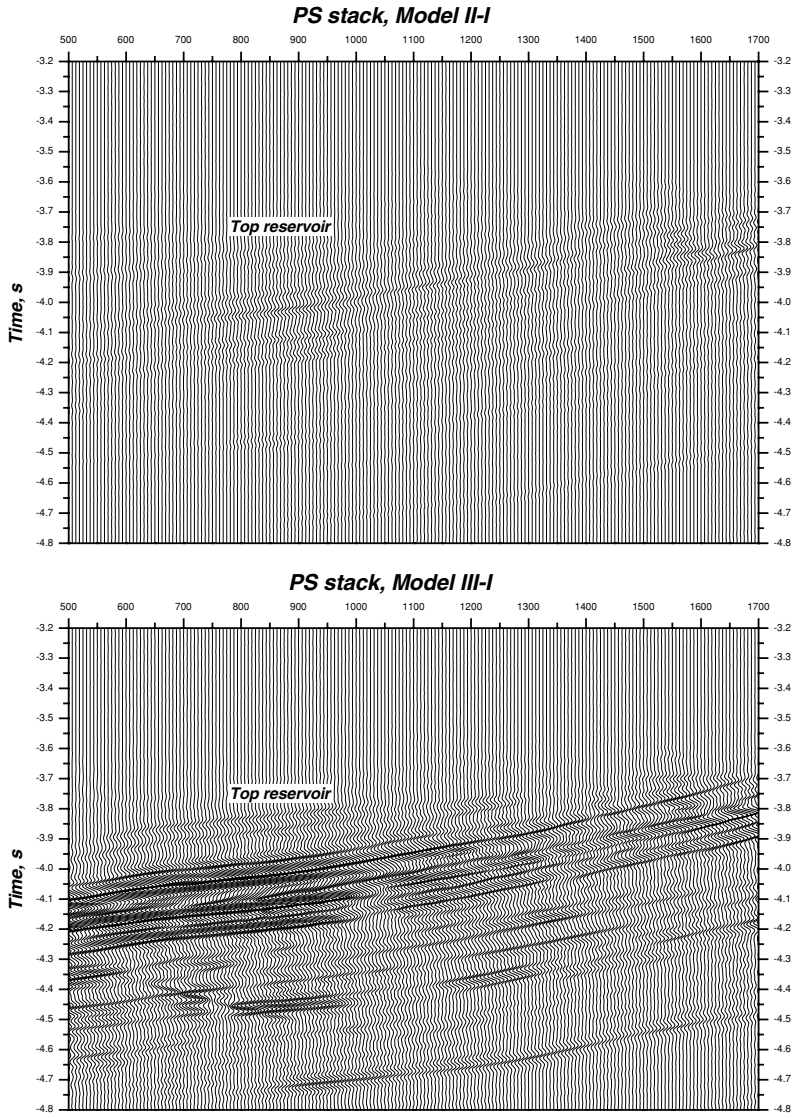

Figure 13. Difference plot for PS stacks from models II and I (to the top) and models III and I (to the bottom).

Testing the proposed method on a synthetic dataset

To test this approach on synthetic data three models, model I, model II and model III, related to the Gullfaks Field were chosen (Arntsen 2002). To model both PP and PS synthetic seismic gathers we use the Ricker wavelet with the central frequency of 30 Hz. Model I has a known initial condition which is based on well log data, while the fluid-pressure conditions for models II and III are based partly on well log observations and partly on fluid flow simulations. For all three models synthetic PP and PS seismic data were generated using a 2D finite-difference algorithm and processed including time migration. Since there was no any specific noise included, the data contain 'the processing noise' only. In practice, the PS data are much more noisy than the PP data. They also have a different frequency bandwidth. These two factors create additional problems for the joint processing and interpretation of PP and PS data. In this study we do not consider any random noise in seismic amplitudes, because introducing the relative PS to PP noise level requires the additional assumptions about the geological model we have used. We assume that all 'random' noise related issues are removed in pre-processing and stacking steps. The processing noise which comes from the finite-difference modelling and following processing, NMO and migration, is also different for PP and PS data. The level of the PS processing noise is always higher than the PP processing noise. In that respect, we believe that to some extent we include the different noise levels for these data with no additional hypothetical assumptions. We also neglect the acquisition differences between PP and PS data, focusing on the pressure–saturation signature only.

The geological structure of the reservoir is shown in figure 2. There are eight types of reservoir rock covering the Tarbert and Ness formations overlaid by shale from the

Table 1. Rock physics parameters have been used to build up the reflection patterns (S_0 is the initial water saturation, K_{fr} is the bulk modulus for solid framework, K_{ma} is the intrinsic modulus of solid, μ is the shear modulus of solid framework, ρ_{ma} is the matrix density and φ is the porosity).

Reservoir unit	S_0	K_{fr} (GPa)	K_{ma} (GPa)	μ (GPa)	ρ_{ma} ($g\ cm^{-3}$)	φ
SM1	0.18	3.27	23.5	3.76	2.52	0.30
SM2	0.11	3.69	22.5	4.14	2.49	0.27
SM3	0.29	4.70	29.0	3.91	2.62	0.29
SM4	0.43	3.93	27.3	4.11	2.60	0.30
SM5	0.69	3.08	29.0	4.82	2.62	0.34
SM6	0.48	5.40	24.0	4.83	2.52	0.23
SM7	0.31	4.02	19.0	3.80	2.42	0.23
SM8	0.74	5.24	23.0	4.55	2.90	0.37

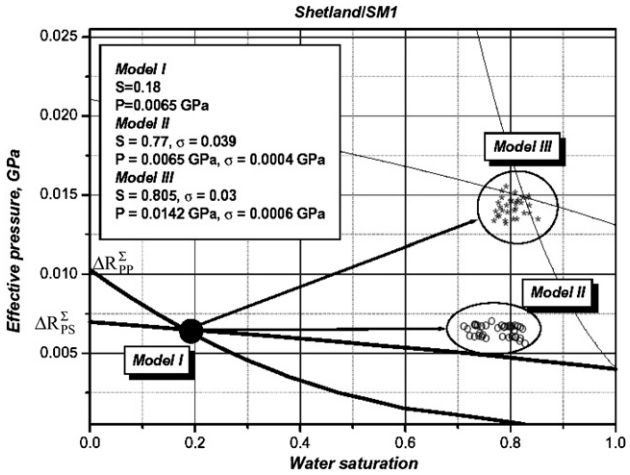

Figure 14. Water saturation–effective pressure discrimination from PP and PS stack data on the reservoir unit SM1. The initial conditions (model I) are given by the crossing of the contours (bold lines crossing the filled circle) related to zero changes in PP and PS amplitudes. The position for each circle is defined by crossing of contours related to changes in PP and PS amplitudes from the difference section (model II–model I) for a given reservoir unit. The star positions are defined in a similar way from the difference section (model III–model I). The statistics (the mean value and the standard deviation) for saturation and pressure estimations for models II and III are listed in the top left. For all other reservoir units these values can be found in table 2.

Shetland formation with bulk modulus of 19.6 GPa, shear modulus of 5.8 GPa and density of 2.3 g cm^{-3}. Reservoir units are named as SM1, SM2, ..., SM8. The rock physics data are given in table 1. Note that different reservoir rocks have different porosities and different initial water saturations. The initial fluid-pressure conditions are given in table 2. The pore pressure is the same for all types of reservoir rocks with an effective pressure of 0.0065 GPa. The effective densities for all reservoir rocks are computed based on the Gassmann model and are dependent on the water saturation. The P-wave and S-wave velocities are dependent on both water saturation and effective pressure. This dependence for the reservoir rocks of the Tarbert formation SM1–SM4 is shown in figures 3 and 4. The P- and S-wave velocities have similar shapes for reservoir units, but numbers are different.

The PP and PS reflection coefficients are computed for the interface between the Shetland formation and the reservoir rocks with initial saturation and pressure conditions which correspond to model I, and plotted versus P-wave incidence angle in figure 5. The stacked PP and PS reflection coefficients are plotted versus P-wave angular span in figure 6. One can see that both PP and PS reflectivities for the reservoir rocks of the Ness formation are less than PP and PS reflectivity for the reservoir rocks of the Tarbert formation.

To build up the reflection pattern we need to estimate the maximum P-wave incidence angle for PP and PS gathers. To do that we use simple ray tracing (figure 7) taking into account the overburden model and maximum offset on PP and PS gathers, which is 2000 m. The typical PP and PS gathers are shown in figure 8. We found that for the maximum offset, the maximum P-wave incidence angle on the PP CMP gather is about 32°, and the maximum P-wave incidence angle on PS CMP gather is about 40°.

The next step is to compute the reflection patterns for the interface between the Shetland formation and each reservoir rock. First we compute PP and PS stacked reflection coefficients assuming a linear correspondence between offset and incident angle and subtract the corresponding values for the initial fluid-pressure conditions. The difference in PP and PS stacked reflection coefficients is then composed into a reflection pattern. These reflection patterns are computed versus water saturation and effective pressure for the interface between the Shetland formation and all reservoir units: Tarbert

Table 2. Results of water saturation and pressure prediction for model II and model III (reservoirs SM1–SM8). N represents the number of points (seismic traces) related to each reservoir unit. The values for saturation and pressure in the headings were used in seismic simulation.

Reservoir unit	N	Model I		Model II ($S = 0.8$, $P = 0.0065$ GPa)				Model III ($S = 0.8$, $P = 0.0145$ GPa)			
		S	P (GPa)	S	σ_S	P (GPa)	σ_P (GPa)	S	σ_S	P (GPa)	σ_P(GPa)
SM1	35	0.18	0.0065	0.77	0.041	0.0065	0.0004	0.805	0.03	0.0142	0.0006
SM2	22	0.11	0.0065	0.825	0.038	0.0053	0.0005	0.802	0.016	0.0146	0.0004
SM3	17	0.29	0.0065	0.828	0.013	0.0056	0.0004	0.807	0.021	0.0145	0.0004
SM4	24	0.43	0.0065	0.83	0.027	0.0061	0.0004	0.8	0.02	0.0146	0.0004
SM5	21	0.69	0.0065	0.8	0.034	0.0065	0.0003	0.8	0.026	0.0146	0.0004
SM6	9	0.48	0.0065	0.81	0.04	0.0069	0.0006	0.771	0.039	0.0146	0.0003
SM7	6	0.31	0.0065	0.789	0.031	0.0058	0.0004	0.767	0.02	0.0145	0.0004
SM8	6	0.74	0.0065	0.78	0.017	0.0067	0.0005	0.796	0.015	0.0146	0.0004

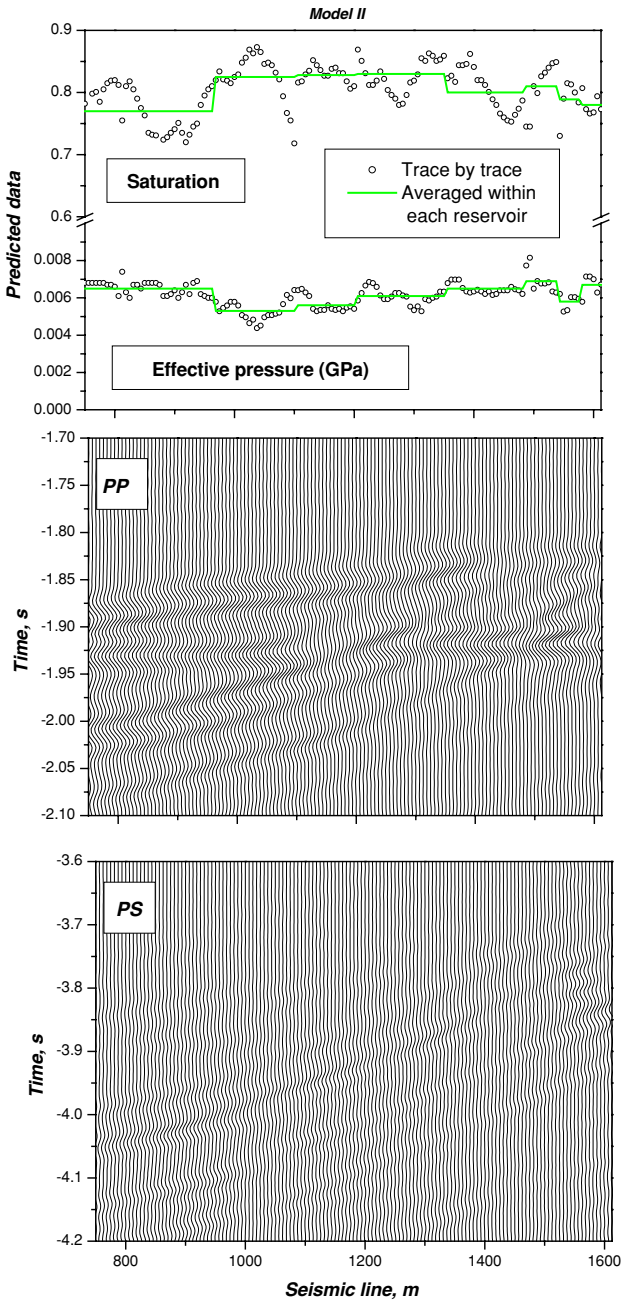

Figure 15. Predicted saturation and pressure (and their mean values within each reservoir unit) plotted along the seismic lines for model II (to the top) and PP (in the middle) and PS (to the bottom) zoomed seismic sections.

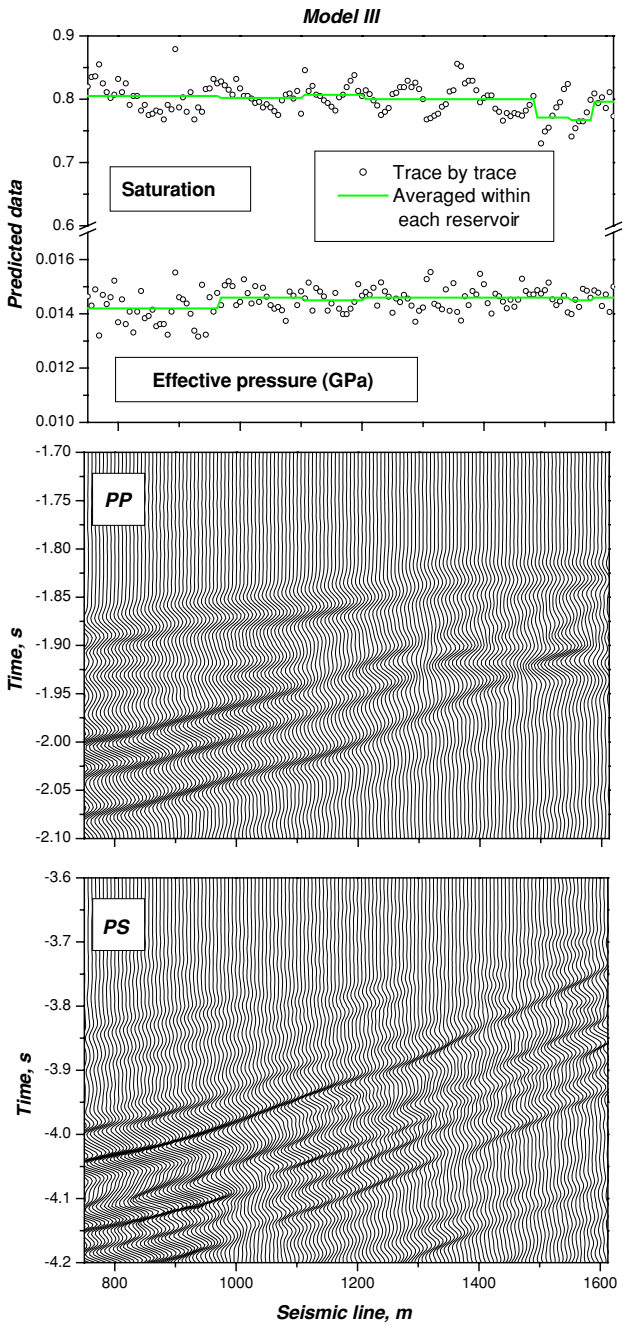

Figure 16. Predicted saturation and pressure (and their mean values within each reservoir unit) plotted along the seismic lines for model III (to the top), PP (in the middle) and PS (to the bottom) zoomed seismic sections.

and Ness formations. The reflection patterns for the reservoir rocks SM1–SM4 are plotted as contour lines in figure 9. The quasi-vertical contour lines are related to the changes in the stacked PP reflection coefficient, while the quasi-horizontal contour lines are related to the changes in the stacked PS reflection coefficient. The thick lines correspond to zero values of $\Delta R^{\Sigma}_{\mathrm{PP}}$ and $\Delta R^{\Sigma}_{\mathrm{PS}}$ for model I. The contour increment is 0.001 for $\Delta R^{\Sigma}_{\mathrm{PP}}$ and 0.0002 for $\Delta R^{\Sigma}_{\mathrm{PS}}$.

Figure 10 shows PP synthetic seismic sections simulated for models I, II and III, respectively. The corresponding PS synthetic seismic sections are shown in figure 11. The difference plots are given in figures 12 and 13 for PP and PS sections, respectively. Note that the difference in PS sections for models III and I is much more pronounced than the difference in PS sections for models II and I.

We use seismic amplitudes from the top reservoir only because the deeper part of the difference section is distorted

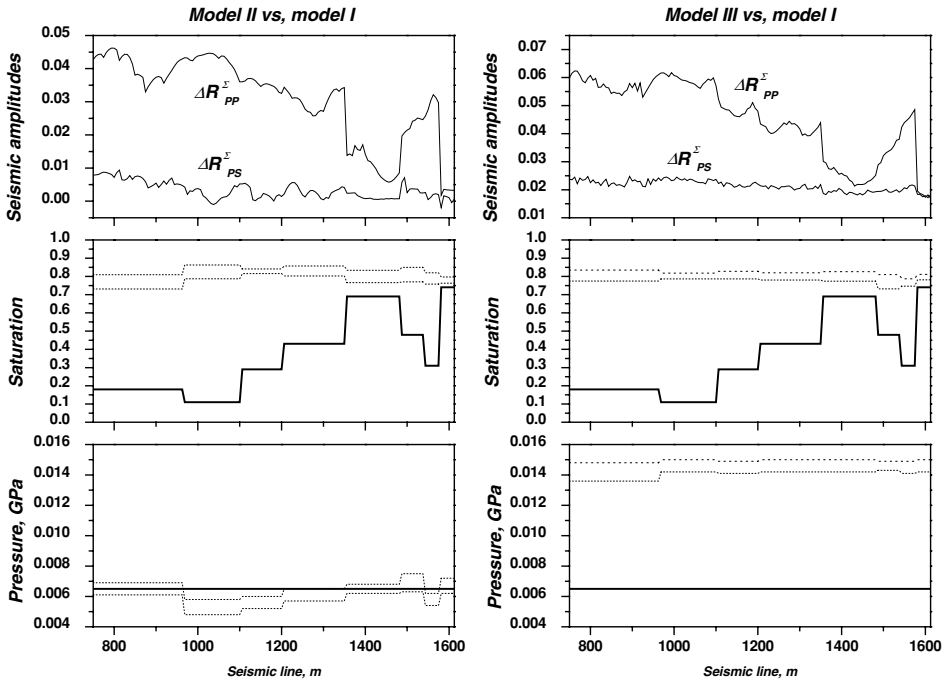

Figure 17. Difference in PP and PS stacked amplitudes and predicted values of saturation and pressure: model II to the left and model III to the right. The solid line on saturation and pressure plots illustrates the initial conditions (model I), while the dash lines show the results of averaging for saturation and pressure plus/minus standard deviation.

due to the complicated phase shift together with the change in interference pattern. This is the result of the velocity and density change due to the change in the fluid-pressure conditions within the reservoir units.

The difference seismic sections are normalized such that the stacked amplitudes of the stacks for model I correspond to the corresponding stacked reflection coefficient for initial saturation and pressure values which are different for different reservoir rocks. Seismic amplitudes along the top reservoir are picked from difference seismic sections, and corresponding contour lines are constructed for the interface between the Shetland formation and each reservoir rock unit. The position of the crossing between the contour lines representing constants $\Delta R^{\Sigma}_{\mathrm{PP}}$ and $\Delta R^{\Sigma}_{\mathrm{PS}}$ gives the values for water saturation and effective pressure (see figure 1). The predictions are given for each type of reservoir rock. An example of the estimation of the fluid-pressure conditions for reservoir unit SM1 is illustrated in figure 14. The circles are related to the crossing of the PP and PS contour lines from the amplitudes on difference sections computed from models I and II, and stars are related to the amplitudes on difference sections computed from models I and III.

The predicted saturation and pressure values are averaged within every reservoir unit. The results for reservoir unit SM1 are shown in figure 14. One can see that models II and III are well separated both in saturation and pressure. The position of data for model II gives an explanation why the difference PS section for models II and I is very weak. For all types of reservoir rock there is a very small change in PS contour lines between these two models. The reflection patterns provide us with interpretation of how saturation and pressure changes affect the seismic PP and PS amplitudes. Nevertheless, we observe that the accuracy prediction goes down if (1) the saturation change is small as for SM5 and SM8 or the change in PP and PS amplitudes is small; (2) there are only few points on the cross-plot as for SM6 and SM7, which means that only few seismic traces represent a given reservoir unit. The noise immunity level decreases with the signal decrease and if there is lack of statistics.

The predicted values of saturation and pressure are plotted together with zoomed PP and PS difference sections for model II (figure 15) and model III (figure 16). The seismic amplitudes from the difference sections and predicted values of saturation and pressure with corresponding uncertainties are shown in figure 17.

To analyse the uncertainties in saturation and pressure the weighting factors from equations (5) and (6) are computed and plotted in figure 18 for all models and reservoir rocks. One can see that the factors responsible for uncertainty in saturation $b_{12}/\det \mathbf{B}$ and $b_{22}/\det \mathbf{B}$ are bigger than the factors responsible for uncertainty in pressure $b_{11}/\det \mathbf{B}$ and $b_{21}/\det \mathbf{B}$. Models II and III, whose difference is the pressure change only, have very similar weighting factors for saturation. The less the difference in saturation between models I and II, the less the difference in weighting factors (reservoir units SM5 and SM8) is.

All results from the prediction are shown in table 2. Maximum errors in prediction for model II are 4% in saturation and 3% in pressure. For model III they are 3% in saturation and 2% in pressure. For realistic cases including noise we expect these prediction errors to increase.

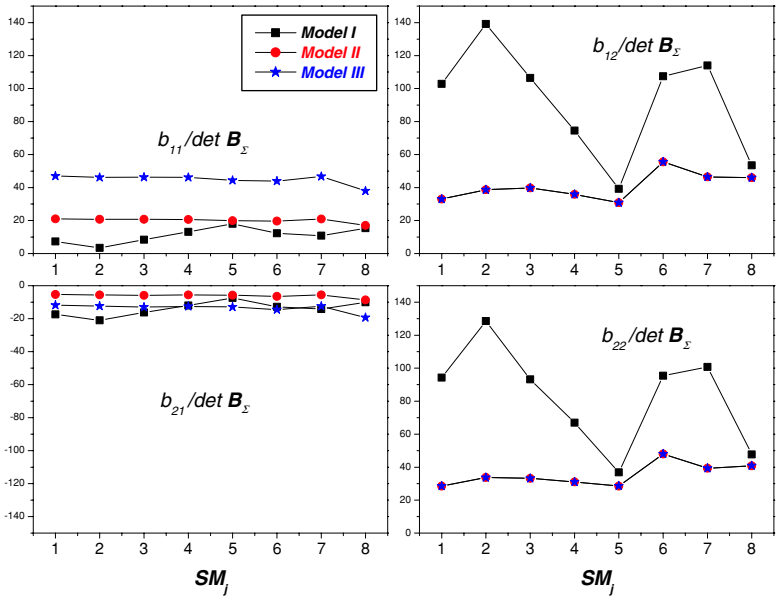

Figure 18. Weighting factors for uncertainties computed for three models and eight reservoir rocks. Factors have been scaled in a similar way. The horizontal axis stays for the index of the reservoir unit. These plots illustrate the sensitivity of the estimation of the effective pressure (to the left) and water saturation (to the right) to the changes in PS amplitudes (to the top) and PP amplitudes (to the bottom).

Uncertainty in estimated parameters

There are two major sources of uncertainty in estimated values for water saturation and pressure. The first one is related to uncertainty in $\Delta R^{\Sigma}_{\mathrm{PP}}$ and $\Delta R^{\Sigma}_{\mathrm{PS}}$ reflection patterns due to uncertainty and variability in rock physics parameters for reservoir units and elastic parameters for the shale unit. The second one is related to the noise in seismic data: structural—from interpretation of the top reservoir, digital—from the limited resolution of seismic data, processing—from insufficient application of processing steps such as hyperbolic normal moveout and finite-difference migration, and residual coherent and incoherent noise. For this study we did not consider any of these effects, focusing on the sensitivity of the method to different parameters for reservoir units. The additional source of uncertainties is poor offset-to-angle conversion due to lack of knowledge about the overburden and the possible tuning due to thinning out of the reservoir. The last effect results in poor estimation of pressure–saturation values for the reservoir unit SM8.

A comprehensive robustness test on the algorithm could consist of the following elements:

(a) Random noise test
(b) Changes in source directivity
(c) Changes in absorption effects (overburden)
(d) Changes in overburden anisotropy
(e) Variation in shale (and sand) rock physics parameters
(f) Changes in reservoir anisotropy (due to fracturing caused by pressure increase)
(g) Changes in geophone coupling (non-random), orientation of the geophone cable, etc.

All the above-mentioned tests would be necessary prior to a field data test, and we have decided to postpone these tests until we have a field dataset to test the algorithm on.

Conclusions

A new method of fluid and pressure discrimination from PP and PS time-lapse seismic stacked data is presented. Plotting contour lines for constant changes in PP and PS reflectivity changes enables us to determine saturation and pressure changes directly. We find that this cross-plotting technique can easily be extended to include uncertainty analysis. The link between reflectivity changes and saturation is the Gassmann model, while the Hertz–Mindlin model (calibrated to rock physics measurements for the given field) is used to account for pressure changes. On a synthetic 2D time-lapse seismic dataset (representing the Gullfaks Field), we find that the proposed method works well in most cases. We find that saturation changes are more sensitive to changes in stacked amplitudes than pressure changes. However, for low effective pressures, we observe that the pressure effect might be much stronger than the fluid effect. The discrimination process is strongly dependent on the *in situ* stress conditions—low effective pressure means low discrimination sensitivity. For a given reservoir, the effect of the difference in the rock physics parameters between the different reservoir units is not crucial for pressure–saturation discrimination. In our study we neglect the effects related to the reflector curvature and the presence of a fault. The uncertainties in the rock physics parameters are also neglected.

References

Andorsen K and Landrø M 2000 Source signature variations versus repeatability—a study based on a zero-offset VSP experiment *J. Seismic Explor.* **9** 61–71

Arntsen B 2002 Finite-difference synthetic data of a model Gullfaks *Statoil Technical Report* N-237B

Brevik I 1999 Rock model based inversion of saturation and pressure changes from time lapse seismic data *69th Annu. Int. Mtg., Soc. Expl. Geophys., Expanded Abstracts* pp 1044–7

Floricich M, MacBeth C and Staples R 2005 An engineering-driven approach for separating pressure and saturation using 4D seismic *Application to a Jurassic Reservoir in the UK North Sea. SEG, Expanded Abstracts* pp 2464–7

Gassmann F 1951 Elastic waves through a packing of spheres *Geophysics* **16** 673–85

Guilbot J and Smith B 2002 4-D constrained depth conversion for reservoir compaction estimation: application to Ekofisk field *The Leading Edge* **21** 302–8

Koster K, Gabriels P, Hartung M, Verbeek J, Deinum G and Staples R 2000 Time-lapse seismic surveys in the North Sea and their business impact *The Leading Edge* **19** 286–93

Landrø M 1999 Repeatability issues of 3-D VSP data *Geophysics* **64** 1673–9

Landrø M 2001 Discrimination between pressure and fluid saturation changes from time-lapse seismic data *Geophysics* **66** 836–44

Landrø M, Digranes P and Strønen L K 2001 Mapping reservoir pressure and saturation changes using seismic methods—possibilities and limitations *First Break* **19** 671–7

Landrø M, Solheim O A, Hilde E, Ekren B O and Strønen L K 1999 The Gullfaks 4D seismic study *Pet. Geosci.* **5** 213–26

Landrø M, Veire H H, Duffaut K and Najjar N 2002 Discrimination between pressure and fluid saturation changes from marine multicomponent time lapse seismic data *Geophysics* **68** 1592–9

Lumley D E and Tura A 1999 Estimating pressure and saturation changes from time-lapse AVO data *69th Annu. Int. Mtg., Soc. Expl. Geophys., Expanded Abstracts* pp 1655–8

MacBeth C, Stammeijer J and Omerod M 2006 Seismic monitoring of pressure depletion evaluated for a United Kingdom continental-shelf gas reservoir *Geophys. Prospect.* **54** 29–47

Meunier J, Huguet F and Meynier P 2001 Reservoir monitoring using permanent sources and vertical receiver antennae: the Cere-la-Ronde case study *The Leading Edge* **20** 622–9

Mindlin R D 1949 Compliance of elastic bodies in contact *J. Appl. Mech.* **16** 259–68

Ritchie B, McGregor A, Strudley A and Goto R 2002 The impact of new 4D seismic technology on the Magnus field *SEG, Expanded Abstracts* pp 544–7

Stovas A M and Landrø M 2004 Optimal use of PP and PS time-lapse stacks for fluid-pressure discrimination *Geophys. Prospect.* **52** 301–12

Stovas A M and Landrø M 2005 Fluid-pressure discrimination in anisotropic reservoir rocks—a sensitivity study *Geophysics* **70** 1–11

Ursin B and Stovas A M 2002 Reflection and transmission responses of a layered isotropic visco-elastic medium *Geophysics* **67** 307–23

Watts G F T, Jizba D, Gawith D E and Gutteridge P 1996 Reservoir monitoring of the Magnus field through 4D time-lapse seismic analysis *Pet. Geosci.* **2** 361–72